



Cite this: DOI: 10.1039/d6sc00616g

All publication charges for this article have been paid for by the Royal Society of Chemistry

# Centimeter-sized single crystals of 3D perovskitoid (4-AP)Pb<sub>2</sub>X<sub>6</sub> (X = Br, I) for efficient and stable X-ray detection

Hongliang Dai,<sup>a</sup> Zeng-Kui Zhu,<sup>\*b</sup> Shihai You<sup>id c</sup> and Junhua Luo<sup>id \*c</sup>

Three-dimensional (3D) metal halide perovskites (MHPs) have been widely studied in the field of X-ray detection, due to their easy synthesis, strong X-ray absorption and high carrier transport capability. However, the conventional 3D ABX<sub>3</sub> MHPs have fatal problems of large dark current drift, severe ion migration and poor environmental stability, which calls for extensive research on the design and modulation of novel 3D perovskitoids to address these issues. In this study, two AB<sub>2</sub>X<sub>6</sub>-type 3D perovskitoids (4-AP)Pb<sub>2</sub>X<sub>6</sub> (4-AP = 4-amidinopyridinium, X = Br, I) with centimeter-sized single crystals have been synthesized for X-ray detection. Thorough studies disclose unique inorganic frameworks composed of both corner-sharing and edge-sharing octahedra, while multi-ammonium aromatic 4-AP<sup>2+</sup> cations are situated within the expansive cavities of the inorganic network. Strikingly, both of these compounds are characterized by elevated activation energy ( $E_a$ ) of ionic conductivity, reduced dark current drift, and superior stability compared to the conventional 3D perovskite MAPbI<sub>3</sub>. In particular, (4-AP)Pb<sub>2</sub>I<sub>6</sub> with a flatter framework achieves a high sensitivity of 2512  $\mu\text{C Gy}^{-1} \text{cm}^{-2}$  and a low detection limit of 0.72  $\mu\text{Gy s}^{-1}$ , due to the better carrier transmission channels and stronger X-ray absorption. This work highlights the potential of the 3D AB<sub>2</sub>X<sub>6</sub> perovskitoid family in high-performance optoelectronics.

Received 22nd January 2026  
Accepted 15th April 2026

DOI: 10.1039/d6sc00616g

rsc.li/chemical-science

## Introduction

Direct X-ray detection, transforming X-ray photons directly into an electrical signal, has great potential for the development of security screening, medical diagnosis, nondestructive determination, computed tomography imaging, *etc.*<sup>1–3</sup> The performance of X-ray detectors is primarily determined by the semiconductors that convert the X-rays into electrical signals. Recent studies show that metal-halide hybrid perovskites offer unique properties including large atomic number ( $Z$ ), high mobility–lifetime product ( $\mu\tau$ ), large resistivity, and fast photo-response, making them promising candidates for high-performance direct X-ray detectors.<sup>4–6</sup> Additionally, the low-cost solution processability makes them attractive for large-scale and disposable applications such as personal dosimetry and medical imaging. Due to the spatial connectivity of the inorganic framework in all three directions, the conventional 3D ABX<sub>3</sub> (A = +1 cations; B = Ge<sup>2+</sup>, Pb<sup>2+</sup>, Sn<sup>2+</sup>; X = Cl<sup>−</sup>, Br<sup>−</sup>, I<sup>−</sup>)

perovskite structure (formed by the corner-sharing motif of the BX<sub>6</sub> octahedra) is preferred because of its fast charge carrier transport, high density and quick response.<sup>7,8</sup> For example, X-ray detectors utilizing MAPbI<sub>3</sub> (MA = CH<sub>3</sub>NH<sub>3</sub><sup>+</sup>) have demonstrated remarkable performance, achieving a sensitivity of  $2.2 \times 10^8 \mu\text{C Gy}^{-1} \text{cm}^{-2}$  and an exceptionally low detection limit of 1.5 nGy s<sup>−1</sup>.<sup>9</sup> Typically, the conventional 3D perovskite structure has defined cages which are stabilized by the so-called Goldschmidt tolerance factor, a geometrical constraint that the A cations in the general formula ABX<sub>3</sub> must satisfy.<sup>10–12</sup> So far, only three +1 A-site cations have been found capable of stabilizing the 3D perovskite frameworks: Cs<sup>+</sup>, MA, and HC(NH<sub>2</sub>)<sub>2</sub><sup>+</sup> (FA).<sup>13,14</sup> In addition to the limited variety of structures, conventional 3D perovskites also have the widespread problems of high dark current drift ( $\sim 10^{-4}$ – $10^{-3}$  nA cm<sup>−1</sup> s<sup>−1</sup> V<sup>−1</sup>), high noise and environmental instability,<sup>15–18</sup> which are not conducive to the realization of practical X-ray detection applications. While significant progress has been made in improving the stability and reducing ion migration in conventional 3D perovskites through surface passivation and compositional engineering,<sup>19,20</sup> structural modification offers an equally effective and fundamentally distinct approach to enhance material performance. Rationally designing the inorganic framework and tailoring the organic–inorganic interactions at the molecular level provides a promising platform to achieve these improvements intrinsically, bypassing the need for post-synthetic treatments or complex device engineering.

<sup>a</sup>School of Chemistry and Chemical Engineering, Key Laboratory of Jiangxi Province for Special Optoelectronic Artificial Crystal Materials, Jingtangshan University, Ji'an, Jiangxi, 343009, China

<sup>b</sup>College of Chemistry and Materials, Jiangxi Province Key Laboratory of Porous Functional Materials, Jiangxi Normal University, Nanchang, Jiangxi, 330022, China. E-mail: zkzhu@jxnu.edu.cn

<sup>c</sup>State Key Laboratory of Functional Crystals and Devices, Fujian Institute of Research on the Structure of Matter, Chinese Academy of Sciences, Fuzhou, Fujian, 350002, China. E-mail: jhluo@fjirm.ac.cn



It is possible to use a dimensionality reduction strategy to construct 2D/1D/0D perovskite detectors with lower dark currents drift and higher stability. This also reduces X-ray absorption and carrier transport efficiency, leading to lower sensitivity, *e.g.* (BA)<sub>2</sub>PbBr<sub>4</sub>:<sup>21</sup> 726.18  $\mu\text{C Gy}^{-1} \text{cm}^{-2}$ ; (BDA)PbI<sub>4</sub>:<sup>22</sup> 242  $\mu\text{C Gy}^{-1} \text{cm}^{-2}$ ; (MPC)<sub>2</sub>PbX<sub>4</sub>:<sup>23</sup> 185  $\mu\text{C Gy}^{-1} \text{cm}^{-2}$ ; (R/S-PPA)<sub>2</sub>BiI<sub>5</sub>:<sup>24</sup> 150  $\mu\text{C Gy}^{-1} \text{cm}^{-2}$ . Thus, the development of novel 3D perovskitoids capable of accommodating larger organic molecules, which not only inherit the high performance of conventional 3D structures but also exhibit better application stability, is therefore in great demand. Fortunately, substituting the B–X octahedral unit in ABX<sub>3</sub> perovskites with a pair of edge-sharing B–X octahedra enables the creation of expanded perovskitoid structures: AB<sub>2</sub>X<sub>6</sub>.<sup>25–27</sup> In 2020, Umeyama *et al.*<sup>13</sup> reported seven members of this new family of materials by synthesizing derivatives with dication pyridinium and ammonium. In the same year, Li *et al.*<sup>14</sup> synthesized four aminomethylpyridinium (AMPY) templated AB<sub>2</sub>X<sub>6</sub> compounds and studied the X-ray detection capability of (3AMPY)Pb<sub>2</sub>I<sub>6</sub>, gaining an X-ray detection sensitivity of 207  $\mu\text{C Gy}^{-1} \text{cm}^{-2}$ . Nevertheless, the impact of halide-modulated molecular assembly on their structure and properties remains largely unexplored. In addition, how to further improve X-ray detection capability through structural modification also remains challenging. As a multi-ammonium aromatic cation, 4-amidinopyridinium (4-AP<sup>2+</sup>) can provide enhanced interactions with the inorganic framework through multiple N–H⋯X hydrogen binding sites, resulting in improved carrier transport and structural stability.<sup>10,28,29</sup> Moreover, the aromatic structure of 4-AP<sup>2+</sup> has a higher dielectric constant than its aliphatic counterparts, which has been considered as an excellent characteristic to improve the optoelectronic performance, *i.e.* better carrier transport and enhanced light absorption.<sup>30–33</sup> In this context, the construction of such 3D perovskitoids using functional 4-AP<sup>2+</sup> is expected to achieve better detection performance.

Herein, templated by 4-AP<sup>2+</sup>, we synthesised two AB<sub>2</sub>X<sub>6</sub>-type 3D perovskitoids (4-AP)Pb<sub>2</sub>Br/I<sub>6</sub> to gain a systematic understanding of their structure–property relationships. Both of them achieved high qualities with centimeter-size single crystals (SC) by a simple solution cooling method. Notably, compared to the conventional MAPbI<sub>3</sub>, they were characterized by elevated activation energy ( $E_a$ ) of ionic conductivity, reduced dark current drift, and superior stability. In particular, the lead iodine counterpart with a flatter inorganic framework and enhanced hydrogen binding has better carrier transmission channels and stronger X-ray absorption, resulting in excellent X-ray detection performance with high sensitivity (2512  $\mu\text{C Gy}^{-1} \text{cm}^{-2}$ ), low detection limit (0.72  $\mu\text{Gy s}^{-1}$ ), and high operational stability. This work provides a deep insight into the potential of the AB<sub>2</sub>X<sub>6</sub> perovskitoid family in high-performance optoelectronics.

## Results and discussion

To avoid the 2D perovskite (4-AP)PbBr/I<sub>4</sub> structures (formed when the ratio of Pb and 4-AP starting materials is 1 : 1), we used a 4 : 1 ratio to obtain the new compounds. All compounds crystallize in the orthorhombic space groups *Pnna*, with the

crystallographic data shown in Table S1. The powder X-ray diffraction (PXRD) results indicate that both (4-AP)Pb<sub>2</sub>Br<sub>6</sub> and (4-AP)Pb<sub>2</sub>I<sub>6</sub> are pure phases (Fig. S1 and S2). As Fig. 1a shows, for (4-AP)Pb<sub>2</sub>Br<sub>6</sub> (the structure of (4-AP)Pb<sub>2</sub>I<sub>6</sub> is similar), two octahedra are linked through edge-sharing to create dimers, which subsequently connect *via* corner-sharing with other dimers, forming continuous layers that extend along the *bc* crystallographic plane. Four edge-sharing dimers are corner-connected across these layers, generating triangular or rectangular voids. These layers, featuring alternating voids, stack along the *a*-axis (stacking direction) through corner connections, ultimately building the anionic inorganic 3D framework (Fig. 1b). An insight into the crystal structure shows that the inorganic framework is formed by two crystallographically independent Pb atoms (Fig. 1c, Pb1 and Pb2). To further investigate the structural difference between (4-AP)Pb<sub>2</sub>Br<sub>6</sub> and (4-AP)Pb<sub>2</sub>I<sub>6</sub>, the structural distortion was examined by calculating the distortion index ( $\Delta d$ , eqn (1)) and bond angle variance ( $\sigma^2$ , eqn (2)), through the variance of the Pb–X bond length and Pb–X–Pb bond angle of the different Pb atoms.

$$D = \frac{1}{6} \sum_i^6 \frac{|l_i - l_{av}|}{l_{av}} \quad (1)$$

$$\sigma^2 = \sum_{i=1}^{12} (\theta_i - 90)^2 / 11 \quad (2)$$

where  $l_i$  is the individual bond length,  $l_{av}$  is the average B–X bond distance, and  $\theta_i$  is the individual bond angle. As Fig. 1d indicates, the  $\Delta d$  and  $\sigma^2$  of both Pb1 and Pb2 are significantly higher in (4-AP)Pb<sub>2</sub>I<sub>6</sub> than those in (4-AP)Pb<sub>2</sub>Br<sub>6</sub>, revealing less structural distortion of (4-AP)Pb<sub>2</sub>I<sub>6</sub>. In addition, the protonated 4-AP provides three N atoms that are directly connected to the inorganic sheets by multiple hydrogen bonds (Fig. 1e). The corresponding 2D fingerprint plot of 4-AP<sup>2+</sup> further shows that the strong N–H⋯I contacts of (4-AP)Pb<sub>2</sub>Br<sub>6</sub> (Fig. 1f) and (4-AP)Pb<sub>2</sub>I<sub>6</sub> (Fig. S3) are distributed over 70.7% and 72.5% of the surface area, respectively. This smoother inorganic framework and enhanced hydrogen interaction of (4-AP)Pb<sub>2</sub>I<sub>6</sub> are likely to result in more favorable charge transport, improved phase stability, and hence improved X-ray detection performance.

The thermogravimetric curves (Fig. 2a) show that (4-AP)Pb<sub>2</sub>Br<sub>6</sub> has high thermal stability up to 246 °C, while (4-AP)Pb<sub>2</sub>I<sub>6</sub> is much more stable up to 278 °C, both of which are superior to the 3D MAPbI<sub>3</sub> (240 °C, Fig. S4). To further investigate the structural stability of the new 3D perovskitoids, the ion migration rate was characterized by the activation energy ( $E_a$ ) of ionic conductivity, which is calculated from its temperature-dependent conductivity curve according to the Nernst–Einstein equation<sup>34</sup> (eqn (3)):

$$\sigma(T) = \left(\frac{\sigma_0}{T}\right) \exp\left(\frac{-E_a}{k_B T}\right) \quad (3)$$

where  $\sigma$  is the conductivity at a given temperature  $T$ ,  $\sigma_0$  is a constant, and  $k_B$  is the Boltzmann constant ( $8.617 \times 10^{-5} \text{ eV K}^{-1}$ ). The conductivities of the SC devices were extracted by fitting the *I*–*V* curves in the high-temperature region (Fig. 2b).



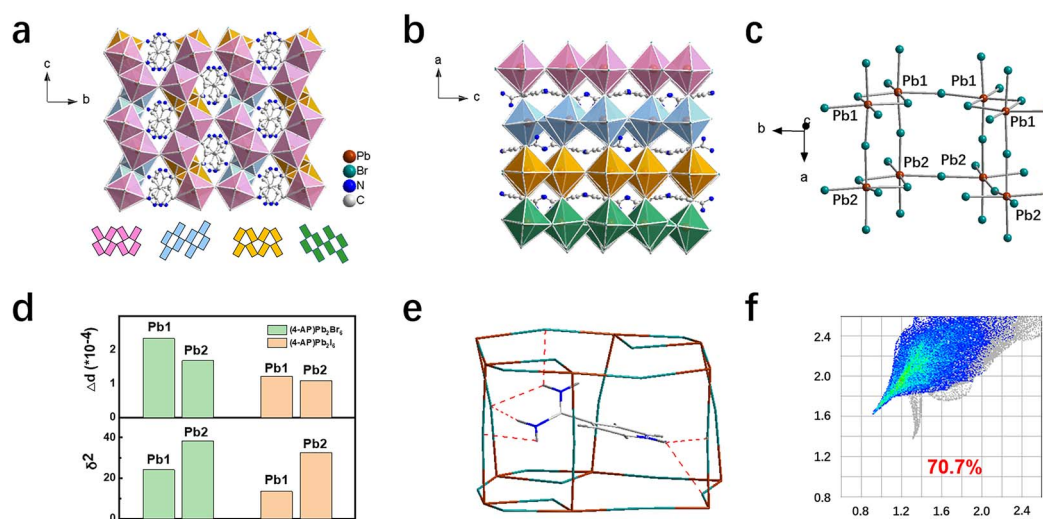


**Fig. 1** (a) The crystal structure of (4-AP)Pb<sub>2</sub>Br<sub>6</sub> viewed from the *a*-axis. The different colors indicate the different inorganic layers. H atoms are omitted for clarity. (b) The crystal structure of (4-AP)Pb<sub>2</sub>Br<sub>6</sub> viewed from the *b*-axis. (c) Fragment of the (4-AP)Pb<sub>2</sub>Br<sub>6</sub> structure showing the coordination environment and connectivity of octahedra. (d) Distortion index ( $\Delta d$ ) and bond-angle variance ( $\sigma^2$ ) of (4-AP)Pb<sub>2</sub>Br<sub>6</sub> and (4-AP)Pb<sub>2</sub>I<sub>6</sub>. (e) Multiple hydrogen bonding between the 4-AP<sup>2+</sup> cation and inorganic framework in (4-AP)Pb<sub>2</sub>Br<sub>6</sub>. (f) 2D fingerprint plots for 4-AP<sup>2+</sup> cations in (4-AP)Pb<sub>2</sub>Br<sub>6</sub>.

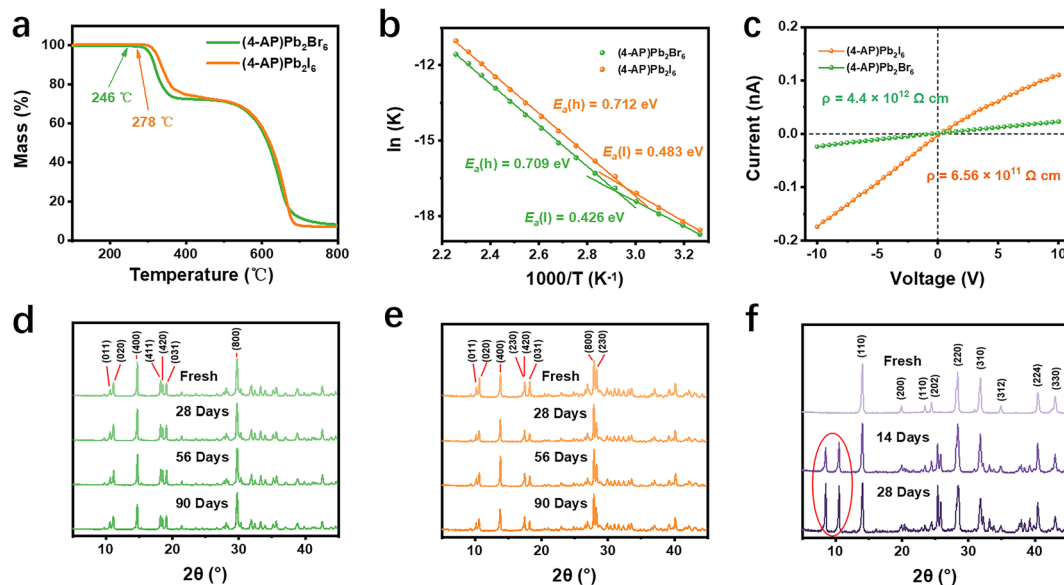


**Fig. 2** (a) The thermogravimetric curves of (4-AP)Pb<sub>2</sub>Br<sub>6</sub> and (4-AP)Pb<sub>2</sub>I<sub>6</sub>. (b) Temperature-dependent conductivities of (4-AP)Pb<sub>2</sub>Br<sub>6</sub> and (4-AP)Pb<sub>2</sub>I<sub>6</sub> SCs. (c) Resistivities of (4-AP)Pb<sub>2</sub>Br<sub>6</sub> and (4-AP)Pb<sub>2</sub>I<sub>6</sub> SCs. (d–f) Experimental powder X-ray diffraction patterns of (4-AP)Pb<sub>2</sub>Br<sub>6</sub> (d), (4-AP)Pb<sub>2</sub>I<sub>6</sub> (e) and MAPbI<sub>3</sub> (f) powder crystals, before and after exposure to the ambient environment (20 ± 10 °C, 70 ± 10% RH).

The ionic conductivity (ion migration) activation energy at high temperature  $E_a(h)$  is calculated to be 0.709 eV for the (4-AP)Pb<sub>2</sub>Br<sub>6</sub> SC, while a slightly higher value of 0.712 eV is observed for the (4-AP)Pb<sub>2</sub>I<sub>6</sub> SC. In contrast, the ion migration is relatively more severe for the MAPbI<sub>3</sub> SC with a lower value of 0.419 eV (Fig. S5), suggesting that by constructing new 3D frameworks, the migration energies become higher and the ion migration is actually inhibited. The low-temperature activation energy  $E_a(l)$  was calculated to be 0.426 eV for (4-AP)Pb<sub>2</sub>Br<sub>6</sub> and 0.483 eV for

(4-AP)Pb<sub>2</sub>I<sub>6</sub>. These values are notably lower than their high-temperature counterparts, which is consistent with previously reported behaviors in hybrid perovskites where low-temperature ion migration is often associated with defect-assisted processes or shallow trap-mediated conduction. The slightly higher  $E_a(h)$  and  $E_a(l)$  observed in (4-AP)Pb<sub>2</sub>I<sub>6</sub> suggests that the flatter inorganic framework and enhanced hydrogen bonding in this compound also effectively suppress ion migration. This dual-regime analysis further corroborates the



superior ion-migration inhibition capability of the 3D perovskitoid structure, particularly in the iodide analogue. Additionally, high resistivity helps minimize dark current and current noise, which are essential for achieving stable and high-performance X-ray detection. Fig. 2c shows the current density–voltage curve, which gives a high bulk resistivity ( $\rho$ ) of  $4.4 \times 10^{12} \Omega \text{ cm}$  for (4-AP)Pb<sub>2</sub>Br<sub>6</sub> and  $6.56 \times 10^{11} \Omega \text{ cm}$  for (4-AP)Pb<sub>2</sub>I<sub>6</sub>. These values are superior to that of commercial CdZnTe ( $10^{10} \Omega \text{ cm}$ ), and over three orders of magnitude higher than that of 3D MAPbI<sub>3</sub> perovskite SCs ( $3.2 \times 10^8 \Omega \text{ cm}$ , Fig. S6). Noteworthily, compared with the MAPbI<sub>3</sub> SCs, the new 3D SCs are phase stable even when exposed to the ambient environment ( $20 \pm 10^\circ \text{C}$ ,  $70 \pm 10\% \text{ RH}$ ) for 90 days. As presented in Fig. 2d and e, the powder X-ray diffraction (XRD) patterns of the ground single-crystal powders of (4-AP)Pb<sub>2</sub>Br<sub>6</sub> and (4-AP)Pb<sub>2</sub>I<sub>6</sub> show no detectable non-perovskitoid diffraction peaks throughout the 90-day ambient exposure period. In contrast, the powder XRD patterns of ground MAPbI<sub>3</sub> single-crystal powders (Fig. 2f) exhibit pronounced new diffraction peaks within just a few days (indicated by red circles), which progressively intensify with prolonged exposure. The additional diffraction peaks correspond to the formation of PbI<sub>2</sub>, which is the final degradation product of MAPbI<sub>3</sub> under ambient conditions.<sup>35,36</sup>

Given the above-mentioned advantages, large SCs were grown through a simple slow temperature cooling process, as shown in the schematic diagram (Fig. 3a and S7). Fig. 3b shows the photographs of the resulting centimeter-scale (4-AP)Pb<sub>2</sub>Br<sub>6</sub> (top, bright yellow crystal) and (4-AP)Pb<sub>2</sub>I<sub>6</sub> SCs (bottom, dark red crystal), with dimensions of  $11 \times 4 \times 3 \text{ mm}^3$  and  $13 \times 4 \times 2 \text{ mm}^3$ , respectively. The SCXRD diffraction spots exhibit strong intensity and precise alignment (Fig. 3c and S8), highlighting the superior crystal quality of these SCs. Additionally, the SEM image in Fig. 3d reveals a remarkably flat and smooth surface for (4-AP)Pb<sub>2</sub>Br<sub>6</sub>, further demonstrating its high crystal quality. The UV-vis absorption spectrum (Fig. S9) displays absorption cutoffs at 470 nm ((4-AP)Pb<sub>2</sub>Br<sub>6</sub>) and 638 nm ((4-AP)Pb<sub>2</sub>I<sub>6</sub>), from

which their optical bandgap can be derived to be 2.75 and 2.04 eV, respectively, according to their corresponding Tauc plots.

Due to the high stability, large bulk resistivity and high quality of these new 3D perovskitoids, two-terminal structures of Ag/SC/Ag X-ray detectors (Fig. 4a, electrode thickness: 2 nm; electrode spacing:  $\sim 5 \text{ mm}$ ) based on SCs were fabricated to further study their X-ray detection performance. The absorption spectra of (4-AP)Pb<sub>2</sub>Br<sub>6</sub> and (4-AP)Pb<sub>2</sub>I<sub>6</sub> and some typical X-ray detection materials ( $\alpha$ -Se, Si and MAPbI<sub>3</sub>) over a wide range of photon energies (10–1000 keV) were simulated based on the photon cross section database, as shown in Fig. 4b. Obviously, the linear absorption coefficients of the new 3D perovskitoids are significantly higher than those of Si and  $\alpha$ -se, indicating their good X-ray attenuation capability. In particular, the linear absorption coefficient of (4-AP)Pb<sub>2</sub>I<sub>6</sub> is even comparable to that of MAPbI<sub>3</sub>, due to its high crystal density and compositional high Z elements, making it well suited for high-performance X-ray detectors. The mobility–lifetime product ( $\mu\tau$ , Fig. 4c) used to evaluate the effectiveness of X-ray detectors is calculated to be  $1.074 \times 10^{-4} \text{ cm}^2 \text{ V}^{-1}$  ((4-AP)Pb<sub>2</sub>Br<sub>6</sub>) and  $1.179 \times 10^{-4} \text{ cm}^2 \text{ V}^{-1}$  ((4-AP)Pb<sub>2</sub>I<sub>6</sub>). These values are comparable to the reported (3AMPY)Pb<sub>2</sub>I<sub>6</sub> device ( $1.2 \times 10^{-4} \text{ cm}^2 \text{ V}^{-1}$ ), demonstrating a promising charge collection performance for X-ray detection applications. Under a bias of 100 V, both detectors show an increased current density with a gradual increase in the X-ray dose rates from 4.35 to 87.66  $\mu\text{Gy s}^{-1}$  (Fig. 4d), while the (4-AP)Pb<sub>2</sub>I<sub>6</sub> detector has a higher current density than that of the (4-AP)Pb<sub>2</sub>Br<sub>6</sub> detector. By fitting their slopes (Fig. S10 and 11), the sensitivity under 100 V is calculated to be  $633 \mu\text{C Gy}^{-1} \text{ cm}^{-2}$  ((4-AP)Pb<sub>2</sub>Br<sub>6</sub>) and  $2512 \mu\text{C Gy}^{-1} \text{ cm}^{-2}$  ((4-AP)Pb<sub>2</sub>I<sub>6</sub>). This result of (4-AP)Pb<sub>2</sub>I<sub>6</sub> is more than 10 times higher than that reported for (3AMPY)Pb<sub>2</sub>I<sub>6</sub> with a value of  $207 \mu\text{C Gy}^{-1} \text{ cm}^{-2}$ , demonstrating the successful performance enhancement by the functional 4-AP<sup>2+</sup>. Furthermore, this result also outperforms most low-dimensional perovskite-based detectors, indicating the superiority of three-dimensional structures.<sup>37–39</sup> The detection ability was then tested under different external bias voltages (e.g. 10, 20, and 50 V), as illustrated in Fig. 4e, where it is evident that sensitivity increases with increasing voltage. We also examined the detection limit, which measures the smallest X-ray dose rate that can be accurately identified. As defined by IUPAC, the limit of detection (LoD) corresponds to the dose rate where the signal-to-noise ratio (SNR) equals 3.<sup>40</sup> By fitting SNRs as a function of dose rates (Fig. 4f), the LoD of (4-AP)Pb<sub>2</sub>Br<sub>6</sub> and (4-AP)Pb<sub>2</sub>I<sub>6</sub> at 100 V is determined to be  $1.49 \mu\text{Gy s}^{-1}$  and  $0.72 \mu\text{Gy s}^{-1}$ , respectively. Both these values are much lower than that of commercial  $\alpha$ -Se film detectors ( $5.5 \mu\text{Gy s}^{-1}$ , with X-ray energy around 20 keV), fully demonstrating their excellent detection capability. Notably, the high sensitivity and low LoD of (4-AP)Pb<sub>2</sub>I<sub>6</sub> are primarily attributable to its higher crystal density (stronger X-ray absorption) and flatter framework (better carrier transmission channels).

Dark current drift ( $I_{\text{drift}}$ ) is another vital parameter of X-ray detectors, where a high value can increase the scattering noise and result in a poor SNR.<sup>18,24</sup> As shown in Fig. 4g, there is a slight dark current drift of  $3.1 \times 10^{-6} \text{ nA cm}^{-1} \text{ s}^{-1} \text{ V}^{-1}$  for (4-AP)Pb<sub>2</sub>Br<sub>6</sub> and  $1.48 \times 10^{-5} \text{ nA cm}^{-1} \text{ s}^{-1} \text{ V}^{-1}$  for (4-AP)Pb<sub>2</sub>I<sub>6</sub> under

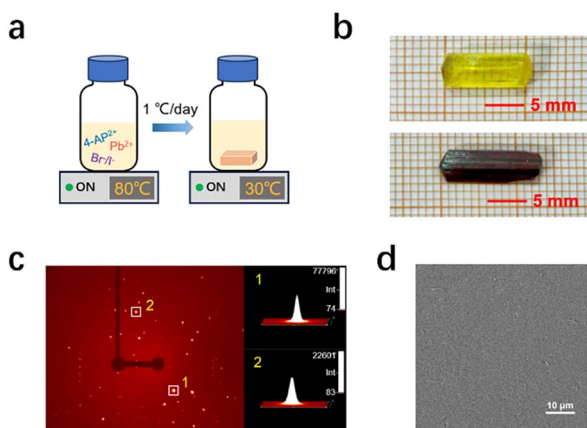


Fig. 3 (a) A schematic showing the growth of SCs. (b) The photos of centimeter-sized SCs of (4-AP)Pb<sub>2</sub>Br<sub>6</sub> (top) and (4-AP)Pb<sub>2</sub>I<sub>6</sub> (bottom). (c) SCXRD diffraction spots of (4-AP)Pb<sub>2</sub>Br<sub>6</sub>. (d) The SEM image of the crystal surface of (4-AP)Pb<sub>2</sub>Br<sub>6</sub>.



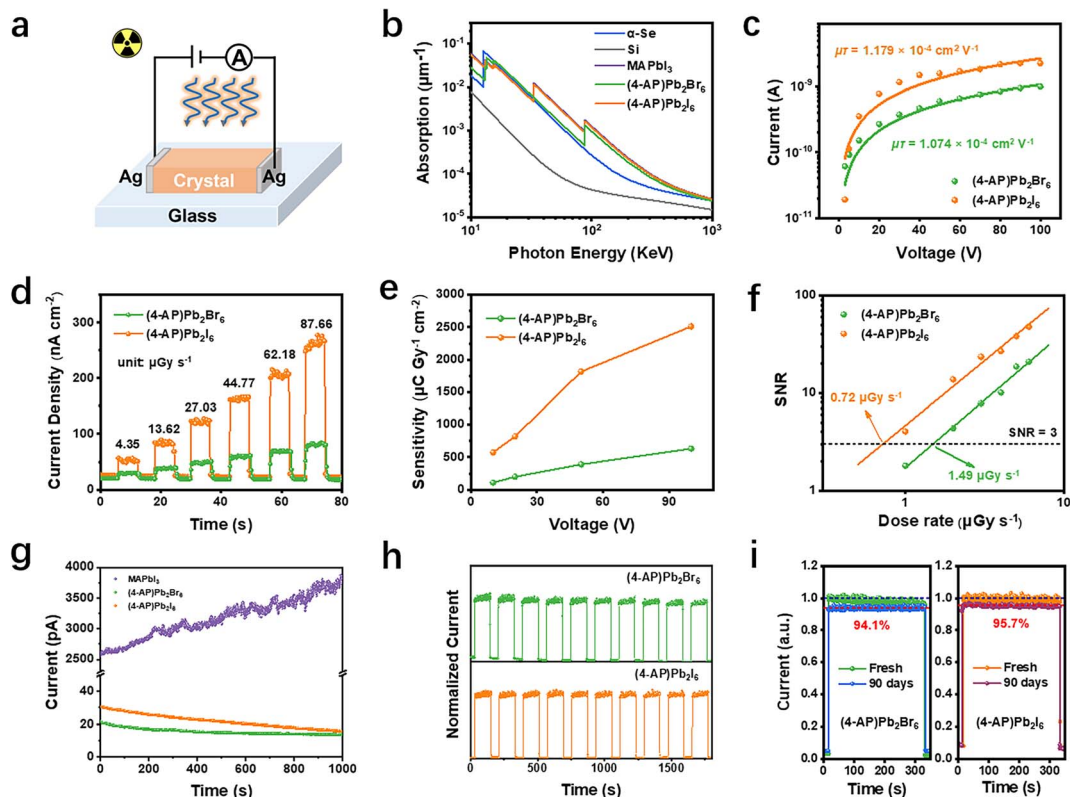


Fig. 4 (a) Schematic diagram of the X-ray photodetector based on single crystals (electrode thickness: 1 mm, electrode spacing:  $\sim 1$  mm). (b) Absorption coefficients of (4-AP)Pb<sub>2</sub>Br<sub>6</sub> and (4-AP)Pb<sub>2</sub>I<sub>6</sub> in comparison to  $\alpha$ -Se, Si and MAPbI<sub>3</sub>. (c) The voltage-dependent photoconductivity of (4-AP)Pb<sub>2</sub>Br<sub>6</sub> and (4-AP)Pb<sub>2</sub>I<sub>6</sub> under X-ray irradiation. (d) Photocurrent response of (4-AP)Pb<sub>2</sub>Br<sub>6</sub> and (4-AP)Pb<sub>2</sub>I<sub>6</sub> detectors to X-ray with increasing dose rates under a bias voltage of 100 V. (e) Sensitivity of (4-AP)Pb<sub>2</sub>Br<sub>6</sub> and (4-AP)Pb<sub>2</sub>I<sub>6</sub> detectors at different bias voltages. (f) Signal-to-noise ratio (SNR) of (4-AP)Pb<sub>2</sub>Br<sub>6</sub> and (4-AP)Pb<sub>2</sub>I<sub>6</sub> detectors at 100 V. (g) Dark current measurements of MAPbI<sub>3</sub>, (4-AP)Pb<sub>2</sub>Br<sub>6</sub> and (4-AP)Pb<sub>2</sub>I<sub>6</sub> detectors under 10 V. (h) Stability results of (4-AP)Pb<sub>2</sub>Br<sub>6</sub> and (4-AP)Pb<sub>2</sub>I<sub>6</sub> detectors exposed to on-off X-ray irradiation in a test period of 10 times under 100 V and 167.9  $\mu\text{Gy s}^{-1}$  doses. (i) Stability measurement of the (4-AP)Pb<sub>2</sub>Br<sub>6</sub> and (4-AP)Pb<sub>2</sub>I<sub>6</sub> detectors in the ambient environment ( $20 \pm 10$  °C,  $70 \pm 10\%$  RH).

10 V. Both are much lower than the that of conventional 3D perovskite SC X-ray detectors, including MAPbI<sub>3</sub> ( $1.18 \times 10^{-3}$  nA cm<sup>-1</sup> s<sup>-1</sup> V<sup>-1</sup>), MAPbBr<sub>3</sub> ( $4.9 \times 10^{-3}$  nA cm<sup>-1</sup> s<sup>-1</sup> V<sup>-1</sup>), MAPbCl<sub>3</sub> ( $5.8 \times 10^{-3}$  nA cm<sup>-1</sup> s<sup>-1</sup> V<sup>-1</sup>) and CsPbBr<sub>3</sub> ( $1.9 \times 10^{-4}$  nA cm<sup>-1</sup> s<sup>-1</sup> V<sup>-1</sup>).<sup>17,18</sup> Such a low  $I_{\text{drift}}$  can be attributed to the effectively suppressed ion migration resulting from the unique framework in the novel 3D perovskitoids.<sup>41</sup> In addition, both the detectors show excellent on-off and long-term irradiation stability, as shown in Fig. 4h, where we applied ten times cycles of “on/off” X-ray irradiation switching over a long period of time under high external bias of 100 V and 167.9  $\mu\text{Gy s}^{-1}$  doses. Storage stability measurement was performed on the detectors under ambient conditions ( $20 \pm 10$  °C,  $70 \pm 10\%$  RH) without any encapsulation. The result shows that the response current of the (4-AP)Pb<sub>2</sub>Br<sub>6</sub> SC detector was still 94.1% of the initial value after 3 months, while the (4-AP)Pb<sub>2</sub>I<sub>6</sub> SC detector retained 95.7% of the response current (Fig. 4i). The above stability test results illustrate the great practical application prospects of these 3D perovskitoid SC-based devices. Table S2 shows a comparison of the performance of the detector (in terms of sensitivity, detection limit, and dark current drift) with a few of

the most representative MHP-based X-ray detectors reported in the literature.

## Conclusions

In summary, by using 4-AP<sup>2+</sup>, we have constructed two AB<sub>2</sub>X<sub>6</sub>-type 3D perovskitoids with centimeter-size single crystals for X-ray detection, which not only inherit the high performance of 3D structures, but also exhibit better stability. Notably, both (4-AP)Pb<sub>2</sub>Br<sub>6</sub> and (4-AP)Pb<sub>2</sub>I<sub>6</sub> exhibit reduced ion migration, reduced dark current drift and enhanced stability compared to the conventional 3D MAPbI<sub>3</sub> analogue, making them excellent candidates for X-ray detection. Changing the halide from Br to I results in higher crystal density, reduced structural distortion and stronger hydrogen bonding in crystal structures and therefore better X-ray absorption and more efficient charge transport. As a result, an efficient X-ray photoresponse was achieved by (4-AP)Pb<sub>2</sub>I<sub>6</sub> with a sensitivity up to 2512  $\mu\text{C Gy}^{-1}$  cm<sup>-2</sup> and a low detection limit of 0.72  $\mu\text{Gy s}^{-1}$ . This work demonstrates that the large single crystals of 3D AB<sub>2</sub>X<sub>6</sub> perovskitoids provide a promising platform for high performance optoelectronics. Although carrier transport pathways in single



crystals are more ordered, making it easier to achieve high-performance X-ray detection, growing single crystals of large dimensions remains extremely challenging. Looking forward, the future development of thin-film or flexible configurations based on these perovskitoids holds promise for expanding their utility into large-area and wearable X-ray detectors.

## Author contributions

H. Dai prepared the samples and wrote the manuscript. Z.-K. Zhu and S. You provided suggestions for the project. J. Luo designed and directed this project. All the authors discussed and commented on the manuscript.

## Conflicts of interest

There are no conflicts to declare.

## Data availability

CCDC 2312099 and 2312100 contain the supplementary crystallographic data for this paper.<sup>42a,b</sup>

Additional synthetic, analytical, and crystal data are available in the supplementary information (SI) of this article. Supplementary information is available. See DOI: <https://doi.org/10.1039/d6sc00616g>.

## Acknowledgements

We are grateful for the financial support from the National Natural Science Foundation of China (22435005, 22193042, 22201284, and 21921001), Natural Science Foundation of Jiangxi Province (20252BAC200222), and the Natural Science Foundation of Fujian Province (2023J05076).

## Notes and references

- H. Wu, Y. Ge, G. Niu and J. Tang, Metal Halide Perovskites for X-Ray Detection and Imaging, *Matter*, 2021, **4**, 144–163.
- Z. Li, F. Zhou, H. Yao, Z. Ci, Z. Yang and Z. Jin, Halide perovskites for high-performance X-ray detector, *Mater. Today*, 2021, **48**, 155–175.
- A. Jana, S. Cho, S. A. Patil, A. Meena, Y. Jo, V. G. Sree, Y. Park, H. Kim, H. Im and R. A. Taylor, Perovskite: Scintillators, direct detectors, and X-ray imagers, *Mater. Today*, 2022, **55**, 110–136.
- Y. Wu, J. Feng, Z. Yang, Y. Liu and S. F. Liu, Halide Perovskite: A Promising Candidate for Next-Generation X-Ray Detectors, *Adv. Sci.*, 2022, **10**, e2205536.
- Y. Zhou, J. Chen, O. M. Bakr and O. F. Mohammed, Metal Halide Perovskites for X-ray Imaging Scintillators and Detectors, *ACS Energy Lett.*, 2021, **6**, 739–768.
- H. Wei and J. Huang, Halide lead perovskites for ionizing radiation detection, *Nat. Commun.*, 2019, **10**, 1066.
- A. Jaffe, Y. Lin, C. M. Beavers, J. Voss, W. L. Mao and H. I. Karunadasa, High-Pressure Single-Crystal Structures of 3D Lead-Halide Hybrid Perovskites and Pressure Effects on their Electronic and Optical Properties, *ACS Cent. Sci.*, 2016, **2**, 201–209.
- J. Wu, L. Wang, A. Feng, S. Yang, N. Li, X. Jiang, N. Liu, S. Xie, X. Guo, Y. Fang, Z. Chen, D. Yang and X. Tao, Self-Powered FA<sub>0.55</sub>MA<sub>0.45</sub>PbI<sub>3</sub> Single-Crystal Perovskite X-Ray Detectors with High Sensitivity, *Adv. Funct. Mater.*, 2021, **32**, 2109149.
- Y. Song, L. Li, W. Bi, M. Hao, Y. Kang, A. Wang, Z. Wang, H. Li, X. Li, Y. Fang, D. Yang and Q. Dong, Atomistic Surface Passivation of CH<sub>3</sub>NH<sub>3</sub>PbI<sub>3</sub> Perovskite Single Crystals for Highly Sensitive Coplanar-Structure X-Ray Detectors, *Research*, 2020, **2020**, 5958243.
- X. Li, J. M. Hoffman and M. G. Kanatzidis, The 2D Halide Perovskite Rulebook: How the Spacer Influences Everything from the Structure to Optoelectronic Device Efficiency, *Chem. Rev.*, 2021, **121**, 2230–2291.
- G. Kieslich, S. Sun and A. K. Cheetham, Solid-state principles applied to organic–inorganic perovskites: new tricks for an old dog, *Chem. Sci.*, 2014, **5**, 4712–4715.
- W. Travis, E. Glover, H. Bronstein, D. Scanlon and R. Palgrave, On the application of the tolerance factor to inorganic and hybrid halide perovskites: a revised system, *Chem. Sci.*, 2016, **7**, 4548–4556.
- D. Umeyama, L. Leppert, B. A. Connor, M. A. Manumpil, J. B. Neaton and H. I. Karunadasa, Expanded Analogs of Three-Dimensional Lead-Halide Hybrid Perovskites, *Angew. Chem., Int. Ed.*, 2020, **59**, 19087–19094.
- X. Li, Y. He, M. Kepenekian, P. Guo, W. Ke, J. Even, C. Katan, C. C. Stoumpos, R. D. Schaller and M. G. Kanatzidis, Three-Dimensional Lead Iodide Perovskitoid Hybrids with High X-ray Photoresponse, *J. Am. Chem. Soc.*, 2020, **142**, 6625–6637.
- S. Shrestha, R. Fischer, G. J. Matt, P. Feldner, T. Michel, A. Osvet, I. Levchuk, B. Merle, S. Golkar, H. Chen, S. F. Tedde, O. Schmidt, R. Hock, M. Ruehrig, M. Goeken, W. Heiss, G. Anton and C. J. Brabec, High-performance direct conversion X-ray detectors based on sintered hybrid lead triiodide perovskite wafers, *Nat. Photonics*, 2017, **11**, 436.
- S. Yakunin, D. N. Dirin, Y. Shynkarenko, V. Morad, I. Cherniukh, O. Nazarenko, D. Kreil, T. Nausser and M. V. Kovalenko, Detection of gamma photons using solution-grown single crystals of hybrid lead halide perovskites, *Nat. Photonics*, 2016, **10**, 585–589.
- Y. He, L. Matei, H. J. Jung, K. M. McCall, M. Chen, C. C. Stoumpos, Z. Liu, J. A. Peters, D. Y. Chung, B. W. Wessels, M. R. Wasielewski, V. P. Dravid, A. Burger and M. G. Kanatzidis, High spectral resolution of gamma-rays at room temperature by perovskite CsPbBr<sub>3</sub> single crystals, *Nat. Commun.*, 2018, **9**, 1609.
- Y. Liu, Z. Xu, Z. Yang, Y. Zhang, J. Cui, Y. He, H. Ye, K. Zhao, H. Sun, R. Lu, M. Liu, M. G. Kanatzidis and S. Liu, Inch-Size 0D-Structured Lead-Free Perovskite Single Crystals for Highly Sensitive Stable X-Ray Imaging, *Matter*, 2020, **3**, 180–196.
- M. Girolami, F. Matteocci, S. Pettinato, V. Serpente, E. Bolli, B. Paci, A. Generosi, S. Salvatori, A. Di Carlo and D. M. Trucchi, Metal-Halide Perovskite Submicrometer-



- Thick Films for Ultra-Stable Self-Powered Direct X-Ray Detectors, *Nano-Micro Lett.*, 2024, **16**, 168.
- 20 W. Zhang, H. Wang, Z. Chen, P. Wang, X. Liu, H. Dong, J. Zhao, Y. Cui and Y. Shao, High-Performance and Stable Perovskite X-ray Detection and Imaging Based on a Ti Cathode, *ACS Appl. Mater. Interfaces*, 2024, **16**, 12844–12852.
- 21 X. Xu, Y. Wu, Y. Zhang, X. Li, F. Wang, X. Jiang, S. Wu and S. Wang, Two-Dimensional Perovskite Single Crystals for High-Performance X-ray Imaging and Exploring MeV X-ray Detection, *Energy Environ. Mater.*, 2023, e12487.
- 22 Y. Shen, Y. Liu, H. Ye, Y. Zheng, Q. Wei, Y. Xia, Y. Chen, K. Zhao, W. Huang and S. F. Liu, Centimeter-Sized Single Crystal of Two-Dimensional Halide Perovskites Incorporating Straight-Chain Symmetric Diammonium Ion for X-Ray Detection, *Angew. Chem., Int. Ed.*, 2020, **59**, 14896–14902.
- 23 J. Wang, J.-H. Yang, J. Chen, S.-H. Wang, Y.-J. Chen and G. Xu, 1D Pb halide perovskite-like materials for high performance X-ray detection, *Chem. Commun.*, 2024, **60**, 3311–3314.
- 24 S. You, Z. K. Zhu, S. Dai, J. Wu, Q. Guan, T. Zhu, P. Yu, C. Chen, Q. Chen and J. Luo, Inch-Size Single Crystals of Lead-Free Chiral Perovskites with Bulk Photovoltaic Effect for Stable Self-Driven X-Ray Detection, *Adv. Funct. Mater.*, 2023, 2303523.
- 25 H.-Y. Zhang, X.-J. Song, H. Cheng, Y.-L. Zeng, Y. Zhang, P.-F. Li, W.-Q. Liao and R.-G. Xiong, A Three-Dimensional Lead Halide Perovskite-Related Ferroelectric, *J. Am. Chem. Soc.*, 2020, **142**, 4604–4608.
- 26 Y.-Y. Tang, Y.-H. Liu, H. Peng, B.-B. Deng, T.-T. Cheng and Y.-T. Hu, Three-Dimensional Lead Bromide Hybrid Ferroelectric Realized by Lattice Expansion, *J. Am. Chem. Soc.*, 2020, **142**, 19698–19704.
- 27 X. Li, M. Kepenekian, L. Li, H. Dong, C. C. Stoumpos, R. Seshadri, C. Katan, P. Guo, J. Even and M. G. Kanatzidis, Tolerance Factor for Stabilizing 3D Hybrid Halide Perovskitoids Using Linear Diammonium Cations, *J. Am. Chem. Soc.*, 2022, **144**, 3902–3912.
- 28 H. Dai, S. You, H. Ye, T. Zhu and J. Luo, Dion-Jacobson to Alternating-Cations-Interaction Reconstruction toward Narrow Bandgap 2D Aromatic Hybrid Perovskite, *Small*, 2023, **19**, 2304332.
- 29 J. Gong, M. Hao, Y. Zhang, M. Liu and Y. Zhou, Layered 2D Halide Perovskites beyond the Ruddlesden-Popper Phase: Tailored Interlayer Chemistries for High-Performance Solar Cells, *Angew. Chem., Int. Ed.*, 2022, **61**, e202112022.
- 30 Q. Cao, P. Li, W. Chen, S. Zang, L. Han, Y. Zhang and Y. Song, Two-dimensional perovskites: Impacts of species, components, and properties of organic spacers on solar cells, *Nano Today*, 2022, **43**, 101394.
- 31 K. Z. Du, Q. Tu, X. Zhang, Q. Han, J. Liu, S. Zauscher and D. B. Mitzi, Two-Dimensional Lead(II) Halide-Based Hybrid Perovskites Templated by Acene Alkylamines: Crystal Structures, Optical Properties, and Piezoelectricity, *Inorg. Chem.*, 2017, **56**, 9291–9302.
- 32 N. R. Venkatesan, A. Mandi, B. Barraza, G. Wu, M. L. Chabinye and R. Seshadri, Enhanced yield-mobility products in hybrid halide Ruddlesden-Popper compounds with aromatic ammonium spacers, *Dalton Trans.*, 2019, **48**, 14019–14026.
- 33 F. Zhang, H. Lu, J. Tong, J. J. Berry, M. C. Beard and K. Zhu, Advances in two-dimensional organic-inorganic hybrid perovskites, *Energy Environ. Sci.*, 2020, **13**, 1154–1186.
- 34 S. Yang, S. Chen, E. Mosconi, Y. Fang, X. Xiao, C. Wang, Y. Zhou, Z. Yu, J. Zhao and Y. Gao, Stabilizing halide perovskite surfaces for solar cell operation with wide-bandgap lead oxysalts, *Science*, 2019, **365**, 473–478.
- 35 N. V. G. N. Nagy, A. Rahaman, S. K. Kalpathy, T. Thomas, S. T. P. and M. U. Kahaly, Unravelling the environmental degradation mechanism of perovskite thin films, *Mater. Adv.*, 2024, **5**, 6426–6439.
- 36 S. Chen, A. Solanki, J. Pan and T. C. Sum, Compositional and Morphological Changes in Water-Induced Early-Stage Degradation in Lead Halide Perovskites, *Coatings*, 2019, **9**, 535.
- 37 Q. Guan, H. Ye, S. You, Z. K. Zhu, H. Li, X. Liu and J. Luo, Radiation Photovoltaics in a 2D Multilayered Chiral-Polar Halide Perovskite toward Efficient Self-Driven X-Ray Detection, *Small*, 2023, 202307908.
- 38 P. Liu, Y. Xiao, Z. Yang, S. Yu and X. Meng, Two-dimensional hybrid double perovskite (PA)<sub>4</sub>AgBiBr<sub>8</sub> single crystals for X-ray detection, *Opt. Mater.*, 2022, **133**, 112972.
- 39 S. You, P. Yu, J. Wu, Z. K. Zhu, Q. Guan, L. Li, C. Ji, X. Liu and J. Luo, Weak X-Ray to Visible Lights Detection Enabled by a 2D Multilayered Lead Iodide Perovskite with Iodine-Substituted Spacer, *Adv. Sci.*, 2023, e2301149.
- 40 C. Ma, H. Li, M. Chen, Y. Liu, K. Zhao and S. Liu, Water-Resistant Lead-Free Perovskitoid Single Crystal for Efficient X-Ray Detection, *Adv. Funct. Mater.*, 2022, **32**, 2202160.
- 41 Y. Liu, Z. Xu, Z. Yang, Y. Zhang, J. Cui, Y. He, H. Ye, K. Zhao, H. Sun, R. Lu, M. Liu, M. G. Kanatzidis and S. Liu, Inch-Size 0D-Structured Lead-Free Perovskite Single Crystals for Highly Sensitive Stable X-Ray Imaging, *Matter*, 2020, **3**, 180–196.
- 42 (a) CCDC 2312099: Experimental Crystal Structure Determination, 2026, DOI: [10.5517/ccdc.csd.cc2hlxvw](https://doi.org/10.5517/ccdc.csd.cc2hlxvw); (b) CCDC 2312100: Experimental Crystal Structure Determination, 2026, DOI: [10.5517/ccdc.csd.cc2hlxwx](https://doi.org/10.5517/ccdc.csd.cc2hlxwx).

